chemosensors

MDPI

*Article*

# Amplitude-Modulated Virtual Sensing and FPGA-Enabled Accurate Recognition for Multiple Gases Using Electronic Nose

**Mingzhi Jiao [1,2], Junqiang Huang [1,2], Fukao Jia [1,2], Bin Bai [1] and Yu Huo [1,2,*]**

[1] The State and Local Joint Engineering Laboratory of Perception Mine, China University of Mining and Technology, Xuzhou 221116, China; mingzhijiao@cumt.edu.cn (M.J.); ts24060122p31@cumt.edu.cn (J.H.); ts25060174p31@cumt.edu.cn (F.J.); baibin13@yeah.net (B.B.)
[2] School of Information and Control Engineering, China University of Mining and Technology, Xuzhou 221116, China
* Correspondence: yuhuo@cumt.edu.cn

**Abstract**

This work presents an enhanced sensing framework for MEMS gas sensors based on tunable-amplitude periodic modulation, enabling multi-state excitation and feature enrichment without increasing the number of sensing elements. A multi-level periodic driving scheme is introduced to realize sensor virtualization, and the resulting multi-state responses are processed using a short-term baseline-tracking algorithm and a dislocated sparse-sampling strategy to improve feature discrimination. A lightweight multilayer perceptron (MLP) classifier is subsequently optimized and deployed on a field-programmable gate array (FPGA)-based accelerator to enable gas recognition under constrained hardware resources. Experimental results obtained from ternary mixtures of $CH_4$, CO, and $H_2$ demonstrate a classification accuracy of 98.5%, accompanied by a 60% reduction in model size and a fivefold improvement in computational speed on the FPGA accelerator.

**Keywords:** electronic nose; tunable-amplitude modulation; virtual sensor; FPGA acceleration

## 1. Introduction

The concept of the electronic nose (E-nose) emerged in the 1980s, intending to emulating biological olfaction for the identification of gases and volatile organic compounds (VOCs) [1]. Early systems primarily relied on a single-metal-oxide-semiconductor (MOS) sensor [2] and focused on reproducing olfactory perception mechanisms. As gas-sensing technologies evolved, the underlying physicochemical mechanisms of gas-sensor interactions became better understood, leading to the development of diverse sensor types [3]. Consequently, the focus of E-nose research shifted from simple biomimicry toward achieving broader multi-gas detection and intelligent analytical capabilities [4].

Since the 1990s, advances in gas-sensing materials and device structures have broadened the range of sensor types from MOS devices to electrochemical and infrared sensors [4]. This progress promoted the development of multi-sensor arrays, enabling E-nose systems to operate in complex gas environments [5]. However, merely increasing sensor quantity was soon recognized as unsustainable due to rising system cost and redundancy. As a result, research attention shifted toward data-driven feature extraction and pattern-recognition approaches capable of achieving accurate gas discrimination with fewer sensors [6,7]. The introduction of machine learning further accelerated this trend, laying the foundation for modern intelligent E-nose architectures [8]. Since the 2000s, continuous progress in MEMS fabrication, nanomaterials, and pattern-recognition algorithms has substantially

Check for updates

Received: 27 November 2025
Revised: 30 December 2025
Accepted: 28 February 2026
Published: 3 March 2026

**Copyright:** © 2026 by the authors. Licensee MDPI, Basel, Switzerland. This article is an open access article distributed under the terms and conditions of the Creative Commons Attribution (CC BY) license.

improved the performance of E-nose systems [9]. MEMS-based semiconductor gas sensors, in particular, have enabled compact sensor arrays with low power consumption and high integration density, making them well suited for intelligent gas analysis when combined with artificial neural networks (ANNs) [10]. Modern E-nose architectures typically employ arrays of MEMS sensors and apply preprocessing and learning-based models to achieve "brain-inspired" recognition, allowing simultaneous identification and quantification of multiple gases rather than simple odor detection.

In current gas-monitoring systems, multisensor integration is commonly employed to improve response diversity for downstream algorithms [11]. However, increasing the number of sensors inevitably increases power consumption, costs, and system complexity [12]. MEMS semiconductor sensors provide a favorable alternative due to their compact size, low power consumption, and long lifetime [13]. Still they suffer from poor selectivity, as different gases often produce overlapping responses [14]. Efforts to address this limitation follow two routes: improving materials and device structures to enhance intrinsic selectivity [15], and applying machine-learning models to extract discriminative patterns from cross-sensitive responses [16]. Although advanced neural networks have achieved high recognition accuracy, their growing complexity poses challenges for edge deployment in resource-limited environments [17]. These constraints have driven interest in alternative solutions, such as sensor-driving strategies and system-level optimization [18]. Recent work has increasingly focused on single-sensor temperature modulation and multi-feature fusion as practical means of enhancing selectivity. Luo et al. introduced a pulsed-driving strategy that exploits transient responses for low-power gas identification [19]. Lee et al. employed a six-step temperature-modulated microheater platform to enable multigas prediction using a deep learning model [20]. Mei et al. further demonstrated that pulse-modulated operation combined with multi-task feature fusion can significantly improve robustness against noise and drift, achieving high accuracy across multiple VOCs [21]. These studies highlight temperature-modulated driving as a powerful approach to overcome the intrinsic selectivity limitations of single MEMS gas sensors. Beyond modulation design, recent studies have also investigated systematic parameter optimization (e.g., heater-voltage range and waveform settings) to maximize separability, and comprehensive reviews have summarized multi-parameter sensing and feature-extraction pipelines for modulated gas sensors [22,23].

To reduce power consumption, constant-voltage DC heating has been increasingly replaced by pulsed or AC driving in MEMS sensors. Owing to their low thermal inertia, short heating interruptions do not significantly affect the sensing trajectory, enabling duty-cycle control to reduce power. However, feature extraction from raw response signals alone provides limited performance gains, motivating studies that modulate the driving waveform to enrich dynamic response features [24–26]. Various waveforms—including sinusoidal and triangular signals—have been explored to enhance separability among gases [27,28]. However, waveform choice and heater-voltage range strongly affect thermal steady-state reachability and the stability of extracted features, motivating recent work on modulation-range optimization and multi-parameter modulation analysis [22,23]. In general, high-frequency modulation favors stability and energy efficiency, whereas low-frequency modulation yields richer transient features. Despite these benefits, most existing approaches rely on fixed-amplitude waveforms, which prevent the sensor from reaching thermal steady state and introduce unstable transitions. This instability restricts feature expansion and reduces model generalizability. Furthermore, dynamic responses are often fed directly into neural networks, limiting compatibility with models trained under constant-voltage conditions.

Neural network inference poses another practical challenge in E-nose deployment. Although training is typically performed on high-performance workstations, the computational and memory demands of the resulting models often exceed the capabilities of embedded devices required for real-time monitoring [29,30]. FPGA-based accelerators have thus attracted growing interest due to their parallelism, reconfigurability, and favorable energy efficiency. Prior work has implemented Sigmoid approximation and pipelined architectures on FPGAs, albeit with certain accuracy losses [31]. Other studies demonstrated reconfigurable platforms capable of executing multiple models [32] or CNN-based accelerators with improved throughput but limited efficiency [33]. Simplified activation-function approximations have also been explored to reduce hardware overhead [34]. More recently, FPGA-based E-nose systems combining waveform modulation and neural network acceleration have shown promising results for real-time gas classification [35]. FPGA-based gas-monitoring systems have also been demonstrated for fast-response leakage detection, but most focus on threshold-based alarms rather than multi-gas pattern recognition; our work targets multi-class recognition under multi-component mixtures with quantified latency and power [36].

This work introduces a tunable-amplitude periodic-driving strategy for combustible-gas monitoring that enhances feature diversity without increasing the sensor count. The proposed scheme virtualizes each MEMS sensor into multiple operating states, and the resulting multi-state responses are further enhanced through segmented reconstruction and dislocated sparse sampling. To support real-time deployment, a lightweight MLP classifier is optimized and implemented on an FPGA-based accelerator with low power consumption. The overall framework integrates driving-signal design, data preprocessing, model optimization, and hardware acceleration, providing a comprehensive solution for low-cost, real-time combustible-gas recognition.

## 2. Experimental Design

### *2.1. Selection and Analysis of Gas Sensor Array*

To meet the requirements of multi-component combustible gas monitoring, the proposed sensing system was designed to operate in ternary gas environments consisting of methane ($CH_4$ from Xuzhou Special Gas Company, Xuzhou, China), carbon monoxide (CO from Xuzhou Special Gas Company, Xuzhou, China), and hydrogen ($H_2$ from Xuzhou Special Gas Company, Xuzhou, China). During sensor selection, multiple commercial MEMS semiconductor gas sensors from different manufacturers were evaluated to ensure coverage of sensing materials and response characteristics suitable for these target gases. Only sensors capable of stable operation under periodically varying heating conditions were retained. For sensor models without explicitly documented compatibility with non-constant heating, long-term stability tests were conducted in clean air using the proposed driving scheme. Sensors exhibiting noticeable degradation or abnormal baseline drift were excluded. Based on these evaluations, three MEMS sensor models were selected for subsequent experiments. Their key parameters, as provided by the manufacturers under standard test conditions, are summarized in Table 1.

It is well established that the electrical resistance and sensitivity of semiconductor gas sensors strongly depend on operating temperature [37]. In this work, instead of using a constant heating voltage, the sensors are driven by a multi-level amplitude-modulated periodic heating voltage, in which the heating voltage is periodically switched among several discrete amplitude levels. It should be emphasized that this driving strategy does not involve conventional alternating-current (AC) operation. Rather, it employs a periodically switched direct-current heating voltage with well-defined amplitude levels, enabling the sensor to repeatedly reach quasi-steady thermal states at different tempera-

tures. Under amplitude-modulated heating, a single MEMS sensor sequentially operates at multiple temperature-dependent states within each modulation cycle. Because the baseline resistance and response dynamics differ at each heating level, the sensor output can be segmented according to the corresponding heating phases. In this study, the term "virtual sensor" refers to a voltage-dependent operating-state response derived from a single MEMS sensor, rather than an additional physical sensing element. Each operating state provides a distinct response characteristic, and these state-dependent responses are treated as independent sensing channels at the signal-processing level. Figure 1 provides a conceptual illustration of this virtualization principle using a simplified two-level heating example. In this illustration, the sensor alternates between two heating amplitudes, and the corresponding response segments are separated and reconstructed to form two distinct response curves. This example is intended solely to clarify the underlying concept. The practical experimental implementation adopts a three-level amplitude-modulated heating scheme, as shown in Figure 2.

**Table 1.** Parameter table of MEMS gas sensor selection.

| Package Type |  |  |  |
|---|---|---|---|
| Sensor Model | GM-402B | GM-702B | GMV-2021B |
| Target Gas | Methane ($CH_4$) | Carbon monoxide (CO) | Hydrogen ($H_2$) |
| Detection Range (ppm) | 1~10,000 ppm | 5~5000 ppm | 0.1~1000 ppm |
| Sensitivity | $R_0/R_s$ (5000 ppm) $\geq 2$ | $R_0/R_s$ (150 ppm) $\geq 3$ | $R_0/R_s$ (200 ppm) $\geq 5$ |
| Heater Power Consumption (mW) | $\leq$80 mW | $\leq$50 mW | $\leq$50 mW |
| Heater Voltage (V) | 2.8 $\pm$ 0.1 V | 2.5 $\pm$ 0.1 V | 2.5 $\pm$ 0.1 V |

Note: $R_0$ denotes the baseline resistance of the sensor in clean air, and $R_s$ represents the sensor resistance at the specified gas concentration. All parameters are provided according to the manufacturers' datasheets under standard test conditions.

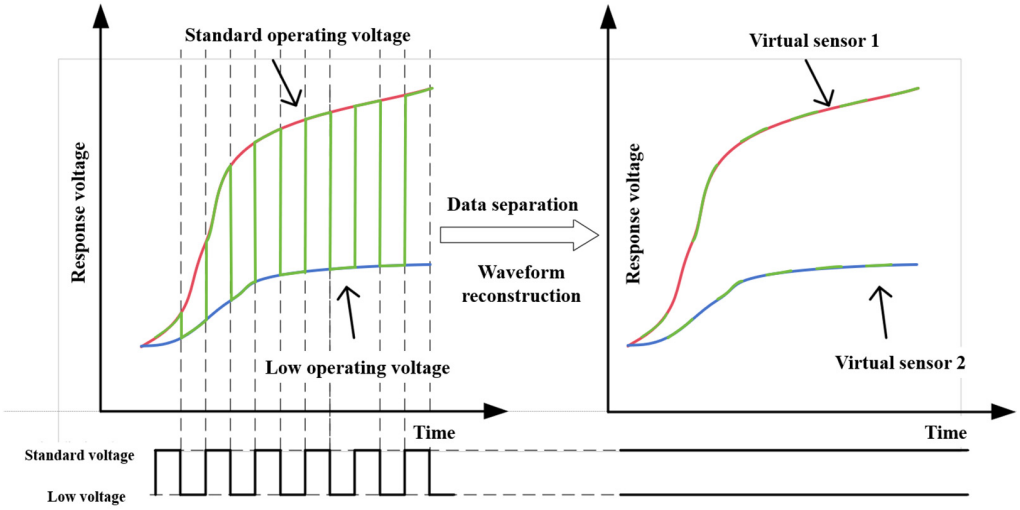



**Figure 1.** Schematic diagram of the virtualization enhancement principle for MEMS gas sensors. Note: The curves in different colors represent the response characteristics of the sensor under the standard operating voltage (red) and the low operating voltage (blue), respectively, while the green curve represents the measured composite response under the alternating driving of the two voltages.

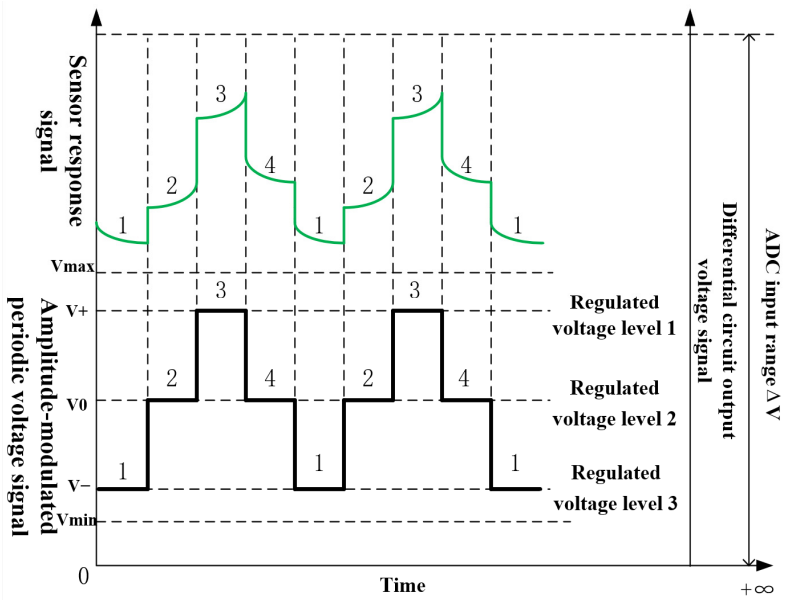



**Figure 2.** Schematic diagram of the three-level tunable-amplitude periodic driving signal and the corresponding sensor response.

According to the manufacturers' datasheets, the optimal heating voltages of the four MEMS sensors employed in this study are 2.8 V, 2.5 V, 2.5 V, and 2.8 V, respectively. For each sensor, the nominal heating voltage $V_0$ is set to its corresponding optimal value to ensure stable operation and reliable gas response. Based on $V_0$, two additional heating levels are generated by applying an upward and downward offset of 0.2 V, forming the three-level amplitude-modulated heating scheme denoted as $V^+$, $V_0$, and $V^-$. Under this three-level modulation, the sensor sequentially experiences multiple quasi-steady operating states and transitional phases, from which four characteristic response segments can be extracted within each modulation cycle. Consequently, a single MEMS sensor can be virtualized into four operating-state-dependent sensing channels.

The sensor response signal shown in Figure 2 represents the measured response voltage across the load resistor connected in series with the chemiresistive sensor, which reflects the resistance change of the sensing material upon gas exposure. The vertical axis therefore corresponds to the response voltage, while the horizontal axis represents time within one modulation cycle. By extending this principle, a k-level amplitude-modulated heating waveform can generate 2 (k − 1) virtual sensing channels from a single MEMS sensor. This approach effectively increases sensing dimensionality without increasing the number of sensing elements, providing enhanced response diversity for subsequent feature extraction and gas recognition. Detailed descriptions of the driving-signal generation circuit, voltage monitoring, and data acquisition hardware are provided in the Supporting Information.

### *2.2. Gas Mixture Configuration*

To evaluate the proposed sensing strategy under realistic multicomponent conditions, ternary gas mixtures of $H_2$, $CH_4$, and CO were prepared according to the procedure outlined in Figure S3 of Supporting Information. To avoid sequence-dependent artifacts during injection, each component was premixed before introduction into the test chamber. A total of 27 ternary mixtures covering a range of volumetric ratios were prepared, and their specific concentrations are provided in Table 2. Following gas premixing, responses from the 27 mixtures were recorded using the acquisition procedure shown in Figure S4 of Supporting Information. Each mixture (label) was measured 15 times to ensure adequate statistical representation. The acquisition board sampled each channel at 1 kHz, and the

12-bit ADC output (0–4095) was stored in time-sequential format. This setup yielded 27 labeled categories with 15 raw response sequences per label. After formatting through the MCU's internal data storage routine, each sensor's response waveform is stored in a .txt file, with data points arranged sequentially by time, values separated by spaces, and line numbers indicating temporal order.

**Table 2.** Injection concentrations of mixed gas samples during testing.

| Gas Label | Injection Concentration (ppm) | | | Gas Label | Injection Concentration (ppm) | | |
|---|---|---|---|---|---|---|---|
| | $CH_4$ | CO | $H_2$ | | $CH_4$ | CO | $H_2$ |
| **1** | 499.00 | 4.99 | 2.00 | **15** | 498.50 | 4.99 | 2.99 |
| **2** | 498.01 | 4.98 | 3.98 | **16** | 399.68 | 6.00 | 0.80 |
| **3** | 497.02 | 4.97 | 5.96 | **17** | 399.36 | 5.99 | 1.60 |
| **4** | 332.89 | 6.66 | 1.33 | **18** | 399.04 | 5.99 | 2.39 |
| **5** | 332.45 | 6.65 | 2.66 | **19** | 749.25 | 2.50 | 1.00 |
| **6** | 332.01 | 6.64 | 3.98 | **20** | 748.50 | 2.50 | 2.00 |
| **7** | 249.75 | 7.49 | 1.00 | **21** | 747.76 | 2.49 | 2.99 |
| **8** | 249.50 | 7.49 | 2.00 | **22** | 599.52 | 4.00 | 0.80 |
| **9** | 249.25 | 7.48 | 2.99 | **23** | 599.04 | 3.99 | 1.60 |
| **10** | 665.78 | 3.33 | 1.33 | **24** | 598.56 | 3.99 | 2.39 |
| **11** | 664.89 | 3.32 | 2.66 | **25** | 499.67 | 5.00 | 0.67 |
| **12** | 664.01 | 3.32 | 3.98 | **26** | 499.33 | 4.99 | 1.33 |
| **13** | 499.50 | 5.00 | 1.00 | **27** | 498.99 | 4.98 | 2.01 |
| **14** | 498.99 | 5.00 | 1.98 | | | | |

## 3. Experiment and Data Processing

The four-channel MEMS array produces four raw response sequences for each gas sample. Under the three-level tunable-amplitude waveform, each sensor experiences four characteristic operating segments, yielding a total of 16 distinguishable response components per sample after segmentation. For an automated combustible-gas monitoring system, it is crucial to capture the sensor response process with high fidelity to generate reliable feature vectors for downstream neural network recognition. Several prior studies have identified response-change thresholds as a means of detecting the onset of gas exposure; however, baseline drift caused by environmental factors such as temperature and humidity often leads to inaccurate detection and frequent false alarms [38]. To improve robustness, baseline-tracking strategies have been proposed to dynamically follow slow drifting trends in sensor signals, thereby enhancing stability and recognition reliability [39]. Building on these advances, this work employs an improved short-term baseline-tracking and response-rate–based identification algorithm that accurately detects and extracts the active response segment from continuous, multi-segment sensor data streams. This method ensures that the reconstructed virtual-sensor signals are consistently aligned to the actual onset of gas response, providing a stable foundation for subsequent preprocessing and classification. Stage identifiers embedded in the data stream allow accurate separation and recombination of the voltage-dependent segments. A moving-average filter is applied to suppress transient artifacts at segment boundaries, generating smooth envelope curves while maintaining dynamic trends. More generally, a k-level driving waveform yields $n = 2(k - 1)$ reconstructed envelopes, thereby expanding each MEMS sensor into multiple virtual sensing channels.

To isolate the active response interval and reduce baseline drift induced by environmental fluctuations, a short-term baseline tracking method was applied. Each reconstructed curve was processed using a sliding window of L = 50 points to update the baseline dynamically. The inter-point voltage difference $\Delta L$ was averaged and time-normalized to

form a response-rate metric $K_1$. When $K_1$ exceeded the adaptive threshold Kparam = 125, the onset of gas response was identified. A fixed-length window of 600 points—beginning 100 points before the detected onset—was extracted as the effective response segment. Given that the virtual sensors operate at an effective sampling rate of 250 Hz, the selected parameters (T = 0.1 and Kparam = 125) provided stable response-onset detection across all 16 reconstructed channels.

Although virtual-sensor reconstruction significantly increases feature diversity, each gas label still provides only 15 samples, which is insufficient for training a neural network without risk of overfitting. To overcome this limitation, a dislocated sparse-sampling augmentation method was developed. From each 600-point segment, a 400-point window (1.6 s) was sparsely sampled at five evenly spaced positions with a 99-point gap. This window was then shifted in steps of 10 points (0.04 s), generating 21 augmented feature vectors per original curve. As a result, the dataset expanded from 405 to 8505 samples while preserving temporal diversity. This augmentation introduces controlled temporal misalignment, enabling the MLP classifier to remain robust to variations of up to 0.8 s in response onset. During real-time inference, feature vectors are produced at 0.04 s intervals and aggregated through majority voting to ensure stable output.

Collectively, the preprocessing pipeline—including multi-level reconstruction, adaptive onset detection, and dislocated sparse sampling—substantially increases dataset richness, alleviates overfitting, and improves robustness in multi-gas classification. Additional implementation details regarding data segmentation and augmentation are provided in Supporting Section S2. Feature vectors extracted from each gas sample were grouped according to their corresponding labels, and the union of all groups formed the final dataset used for model training. The augmented multi-gas feature dataset is visualized in Figure 3, where curves from the 27 mixture categories are shown in distinct colors to highlight inter-class differences.

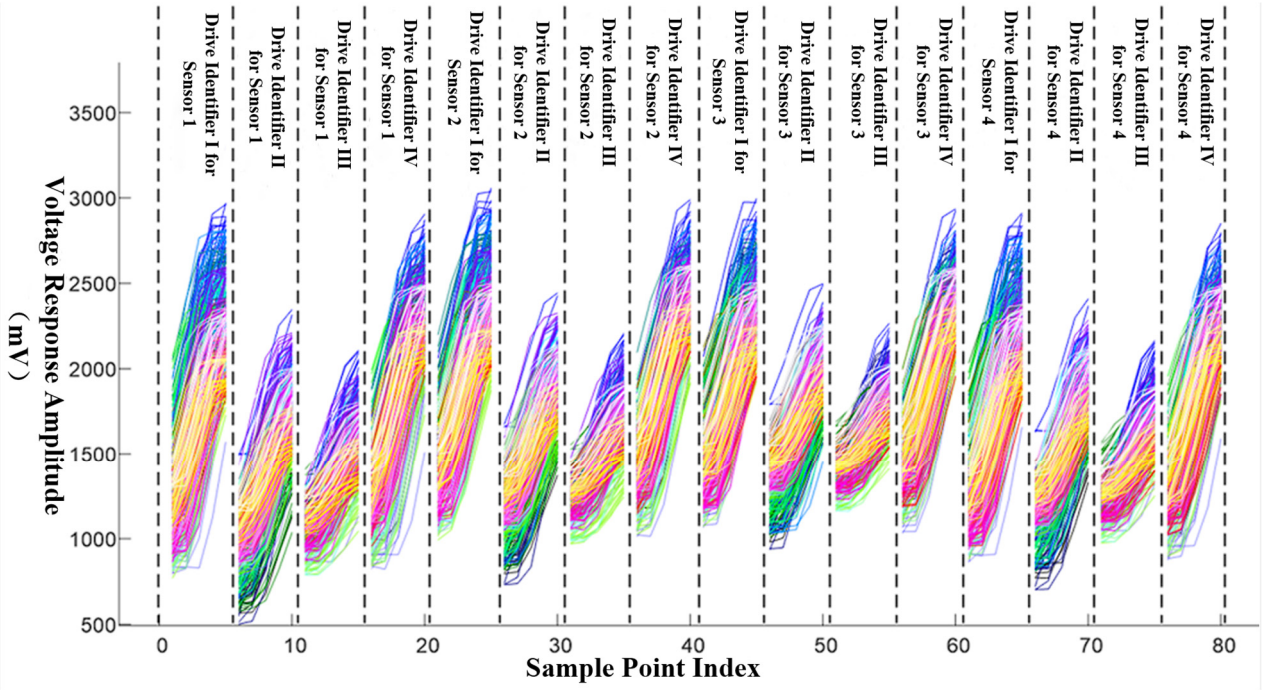



**Figure 3.** Enhanced gas feature dataset. The curves corresponding to the 27 mixture categories are presented in 27 distinct colors to highlight the differences between the categories.

## 4. MLP Network Training and Optimization

### *4.1. Training of the MLP-Based Gas Recognition Network*

The enhanced feature dataset was randomly partitioned into a training set (80%, 6804 samples) and a testing set (20%, 1701 samples). Model hyperparameters—including activation function (ReLU or Sigmoid) and the number of fully connected layers (one to three)—were optimized using a Bayesian search strategy. A five-fold cross-validation procedure was further employed to assess model robustness and ensure stability across different parameter configurations. To quantitatively evaluate the benefit of the proposed enhancement strategy, a control dataset was collected under constant-voltage driving using the same hardware platform. Both datasets were trained under identical hyperparameter constraints to ensure fair comparison. Models achieving test accuracies above 60% were retained for further analysis, and their performance metrics are summarized in Table 3; additional details are available in Table S1 of Supporting Information. Notably, the six highest-performing models were all obtained from the enhancement-based dataset, demonstrating the effectiveness of the proposed reconstruction and sparse-sampling scheme in improving classification accuracy.

**Table 3.** Summary of the training and performance comparison results of gas recognition models in the experimental and control groups. Activation Function R refers to ReLU, while S refers to Sigmoid, NA means not a number.

| Model No. | Test Accuracy (%) | Validation Accuracy (%) | No. of Neurons | | | Activation Function | Enhanced Strategy Applied (Yes/No) |
|---|---|---|---|---|---|---|---|
| | | | Layer 1 | Layer 2 | Layer 3 | | |
| 1 | 99.96 | 99.71 | 22 | 156 | 265 | R | yes |
| 2 | 99.88 | 98.57 | 24 | 97 | NA | S | yes |
| 3 | 99.84 | 99.55 | 103 | 135 | 1 | S | yes |
| 4 | 99.80 | 99.66 | 64 | 156 | 102 | S | yes |
| 5 | 99.61 | 98.27 | 61 | 58 | 143 | R | yes |
| 6 | 99.61 | 99.41 | 25 | 81 | NA | R | yes |
| 7 | 99.18 | 97.95 | 49 | 278 | 291 | S | no |
| 8 | 98.63 | 92.93 | 12 | 300 | NA | R | no |
| 9 | 98.51 | 97.55 | 24 | 58 | 169 | R | no |
| 10 | 97.37 | 98.82 | 63 | 1 | NA | S | yes |
| 11 | 97.02 | 91.28 | 250 | NA | NA | R | yes |
| 12 | 93.53 | 97.75 | 25 | 244 | 300 | R | no |
| 13 | 90.83 | 84.06 | 297 | 1 | NA | S | no |
| 14 | 85.38 | 83.49 | 300 | NA | NA | S | no |
| 15 | 82.36 | 87.37 | 35 | 63 | 1 | S | no |
| 16 | 67.50 | 67.95 | 300 | NA | NA | R | no |

### *4.2. Effectiveness Analysis of the Enhancement Strategy*

Both datasets produced eight candidate models under different hyperparameter settings, and their performances are listed in descending order of test accuracy. As indicated in Table 3, the six highest-performing models originated exclusively from the enhancement-based dataset. This confirms that the tunable-amplitude driving and reconstruction approach effectively increases the discriminative power of the sensing features. Among all 16 models, seven achieved test accuracies above 99%, six of which were from the experimental group. With the threshold set at 95%, the experimental group still outperformed the control group by a ratio of 8:3 while requiring fewer neurons on average. Furthermore, models trained on the enhanced dataset consistently achieved training accuracies above 90%, whereas only eight models in the control group exceeded 60%, highlighting the substantial improvement in data quality and learnability.

In summary, the proposed enhancement strategy not only improves the recognition accuracy of the gas classification models but also substantially reduces the network complexity and neuron count, enabling a more compact and efficient gas monitoring system.

### *4.3. Analysis of Model Prediction Speed and Computational Complexity*

In practical deployment, network size alone does not fully determine computational load. For a single-hidden-layer MLP with $r$ input neurons, $s$ hidden neurons, and t output neurons, each hidden neuron performs $r$ multiplications and $r$ additions, followed by one activation evaluation. Thus, the hidden layer requires $r \times s$ multiply–accumulate operations and $s$ activation computations. This formulation provides a more accurate indication of computational complexity when comparing different model architectures.

Using the above formulation, the computational workload of each trained model was calculated and visualized in Figure 4, which plots the number of multiplication operations and activation evaluations in descending order of test accuracy. Based on accuracy considerations, Models 1 and 2 emerged as top candidates. Model 1 has a larger computational burden than Model 2; however, its runtime performance also depends on implementation factors, such as numerical precision and hardware pipelining. Following the principle of prioritizing test accuracy, the best-performing models are identified as Model 1 and Model 2. Although Model 1 exhibits a significantly larger computational load than Model 2, its actual runtime performance is also influenced by factors such as the effective bit precision of the parameter matrices and hardware-level implementation details.

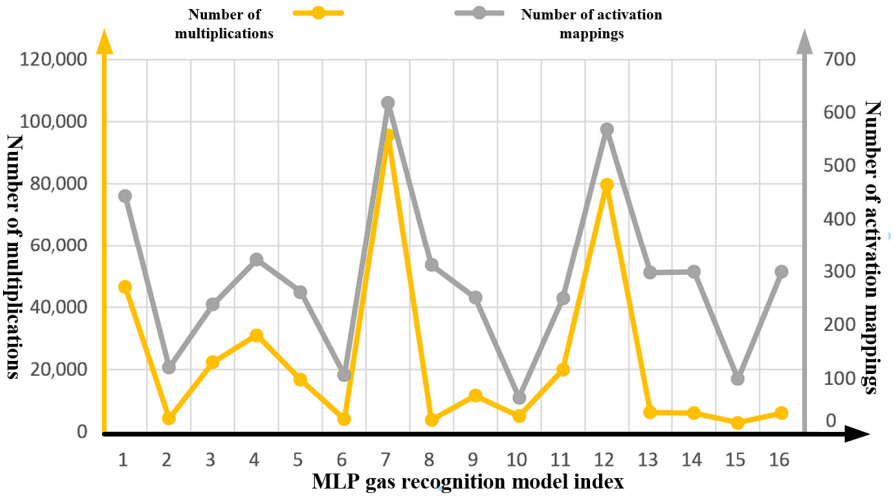



**Figure 4.** Line plots of the numbers of multiplication operations and activation function evaluations.

Figure 5 provides a comprehensive comparison of model performance considering test accuracy, validation accuracy, neuron count, computational complexity, prediction speed, and overall model size. Model 2 offers the best trade-off among these factors, although its slightly lower cross-validation accuracy compared with Models 1 and 3 suggests reduced robustness. Consequently, both Models 1 and 2 were selected for further evaluation, and the superior one was ultimately deployed in the final system.

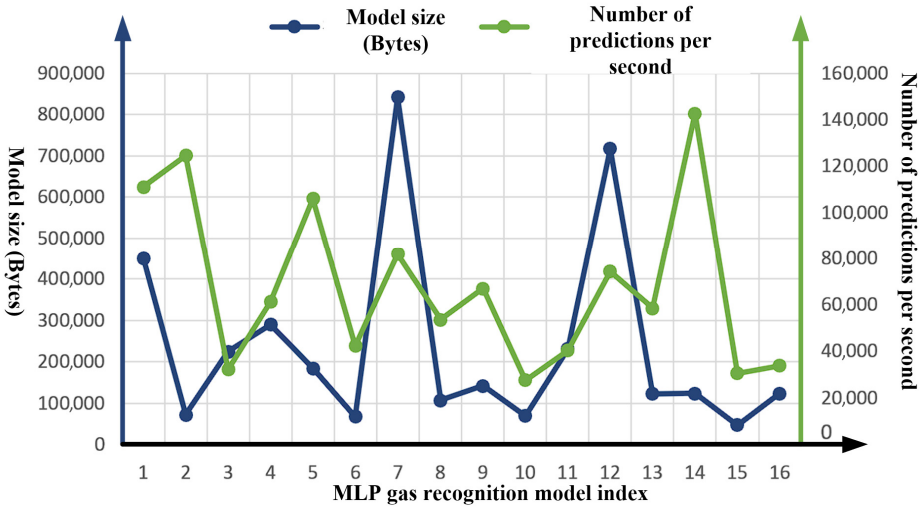



**Figure 5.** Line plots of model size and prediction speed.

### *4.4. Analysis of Neuron Effectiveness in the Model*

During neural-network training process, parameter updates are governed by gradient-based optimization, and both the activation function and regularization strategy strongly influence gradient flow. As training progresses, some neurons may cease to contribute meaningful outputs due to vanishing gradients or weight shrinkage, resulting in constant or near-zero activations. Such neurons—commonly referred to as dead neurons—do not propagate useful information to subsequent layers and therefore increase computational overhead without improving performance. Identifying and pruning these inactive units enables further simplification of the MLP architecture without sacrificing classification accuracy.

Figure 6 illustrates the activation-intensity heat map of Model 1 generated using the enhanced feature dataset. Model 1 comprises three hidden layers, each visualized with a distinct color. Neurons are arranged along the vertical axis, while the horizontal axis corresponds to the evaluation of 8505 test samples. The color scale reflects the activation magnitude of each neuron, enabling direct observation of inactive or consistently zero-valued units.

The heat map shows that each hidden layer contains neurons with persistently zero activations. Their counts are summarized in Table 4. Pruning these units reduces the total number of hidden neurons by 31.6%, demonstrating that a substantial portion of the network does not contribute to the final prediction and can be removed to improve computational efficiency.

**Table 4.** Optimization of dead neurons in Model 1.

| | Initial Neuron Count | Number of Dead Neurons | Optimized Neuron Count | Optimization Ratio (%) |
|---|---|---|---|---|
| Hidden Layer 1 | 22 | 6 | 16 | 27.3 |
| Hidden Layer 2 | 156 | 50 | 106 | 32.1 |
| Hidden Layer 3 | 256 | 81 | 175 | 31.6 |
| Total | 434 | 137 | 297 | 31.6 |

Figure 7 presents the activation-intensity visualization for Model 2, which contains two hidden layers. The primary distinction between Models 1 and 2 is the activation function: Model 1 employs ReLU, whereas Model 2 uses Sigmoid. The Sigmoid function theoretically produces non-zero outputs over its entire input range, leading to fewer strictly inactive neurons but potentially many low-activity neurons with negligible contribution.

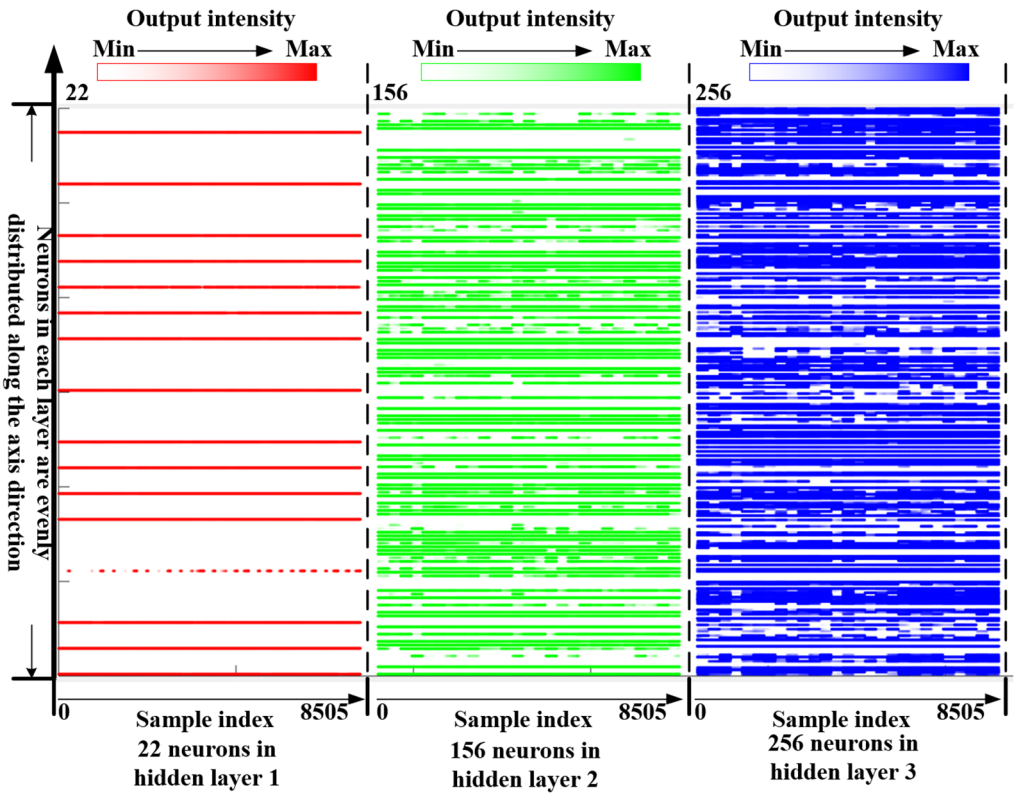



**Figure 6.** Neuron activation intensity heat map of Model 1 on the feature dataset.

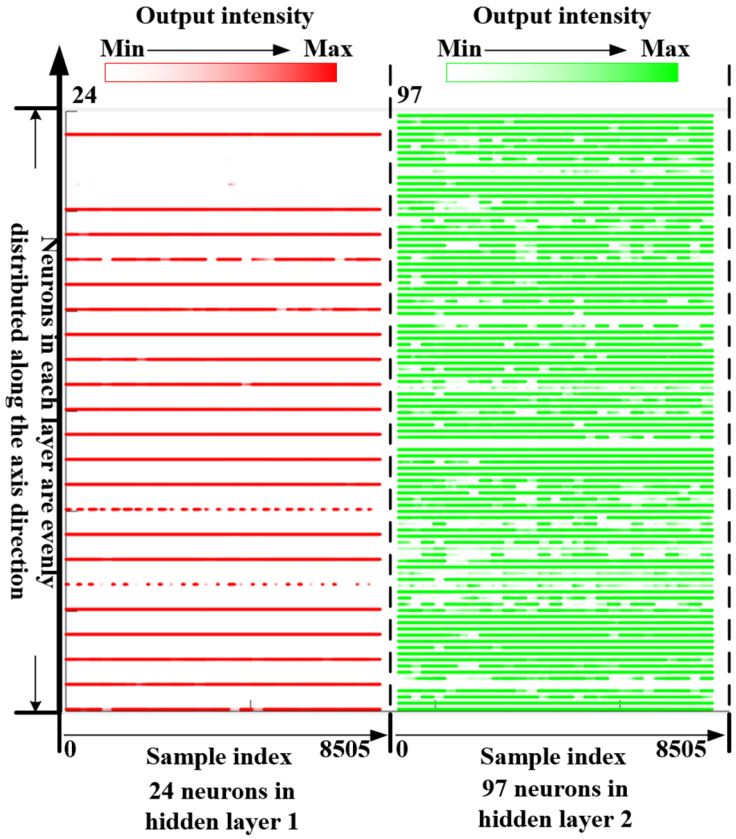



**Figure 7.** Neuron activation intensity heat map of Model 2 on the feature dataset.

Unlike ReLU, which outputs an exact zero for all non-positive inputs, the Sigmoid function generates continuous values in the range (0, 1), asymptotically approaching—

but never reaching—zero. Apparent zero outputs in the heat map result from numerical precision limits rather than true inactivity. Thus, Sigmoid-based networks exhibit low-activity neurons rather than true dead neurons. These neurons contribute little information to downstream layers due to their consistently small activation magnitudes.

During neural network training, regularization constraints cause the neuron weights to converge toward zero, leading to a narrow weight distribution range with limited variation in magnitude. If a neuron's output remains significantly smaller than those of other neurons in the same layer across the entire dataset, the information it transmits to the next layer becomes minimal. Such neurons are referred to as low-activity neurons. Within an acceptable precision loss margin, pruning these low-activity neurons can effectively improve the model's prediction efficiency.

To quantify neuron activity, an average activation measure $E$ was defined:

$$E = \frac{\sum_{i=1}^{n} O_i}{n}$$

where $n$ denotes the total number of test samples and $O_i$ represents the neuron's activation for the $i^{th}$ input. The metric $E$ captures the mean response level of a neuron across the dataset, providing a statistical basis for identifying units with persistently low activation.

Because Sigmoid activations are bounded within (0, 1), the corresponding values of $E$ also lie within this interval. Several threshold values were selected to identify low-activity neurons, and the number of neurons falling below each threshold was quantified. The results, summarized in Table 5, show that a non-negligible subset of neurons exhibits minimal activation and can be pruned with negligible impact on classification accuracy.

**Table 5.** Optimization of low-activity neurons in Model 2.

| | **Initial Neuron Count** | **Number of Low-Activity Neurons** | | |
|---|---|---|---|---|
| | | $E < 0.001$ | $E < 0.005$ | $E < 0.010$ |
| Hidden Layer 1 | 24 | 2 | 2 | 2 |
| Hidden Layer 2 | 97 | 3 | 5 | 8 |
| Total | 121 | 5 | 7 | 10 |
| Optimization Ratio (%) | 0 | 4.1 | 5.7 | 8.2 |

Based on the above observations, the optimal MLP architectures were refined by pruning dead neurons in the ReLU-based model and low-activity neurons in the Sigmoid-based model. This pruning step reduces network size and computational complexity while preserving predictive performance, thereby enhancing the suitability of the models for deployment on resource-constrained embedded platforms.

## 5. Construction and Performance Comparison of MLP Neural Network Accelerator

### *5.1. Structural Analysis of the MLP Neural Network*

The multilayer perceptron (MLP) architecture comprises an input layer, one or more fully connected hidden layers, and an output layer. Nonlinear activation functions allow the MLP to approximate complex input–output relationships, making it suitable for modeling nonlinear gas-response patterns in the proposed sensing framework. Within each hidden or output layer, neurons perform weighted-sum operations followed by bias addition and activation. The computational cost depends strongly on the chosen activation function: ReLU requires only a conditional comparison ($f(x) = \max(0, x)$), whereas Sigmoid involves exponential and division operations ($f(x) = 1/(1 + e^{-x})$). Consequently,

ReLU-based networks are more suitable for hardware acceleration due to their lower arithmetic complexity.

### *5.2. Design of an FPGA-Based MLP Accelerator*

FPGAs support fine-grained parallelism and deep pipelining, providing advantages in latency and energy efficiency for neural-network inference. In this work, a generalized arithmetic module was designed to perform multiply—accumulate operations while minimizing logic utilization. The ReLU activation function was implemented using simple conditional logic to reduce latency, whereas all network parameters were quantized from floating-point to fixed-point formats to further lower hardware complexity and resource consumption. The accelerator corresponding to Model 1 (ReLU-based) was implemented using a state-machine–driven computation pipeline, as shown in Figure S5 of Supporting Information. Operating at 50 MHz, the accelerator achieves an inference latency of 2.175 ms with a total power consumption of 288 mW. Block RAM (BRAM) usage accounts for 35.36% of available resources, primarily due to the storage requirements of weights and biases. Detailed synthesis results and power analysis are provided in Figure 8.

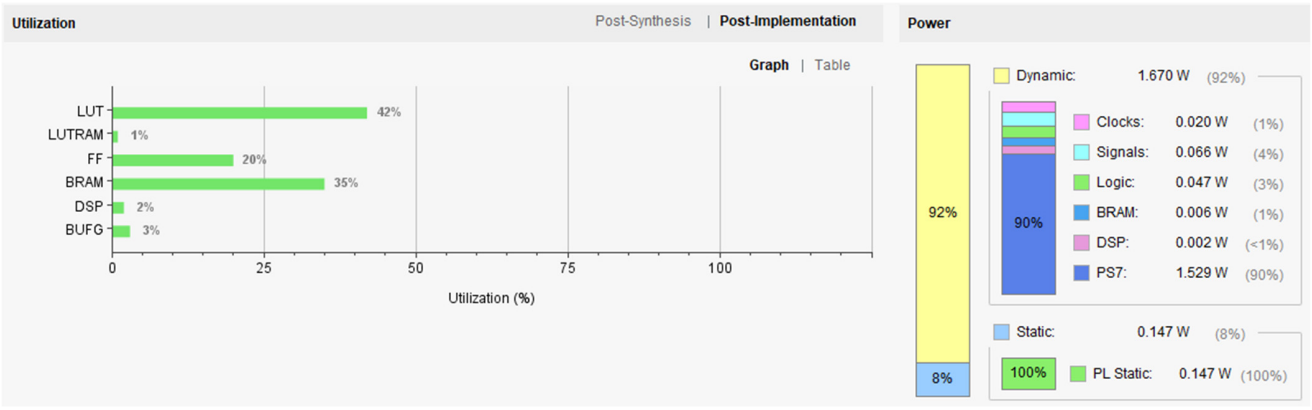



**Figure 8.** Resource utilization and power consumption evaluation of Model 1 accelerator.

Model 2 employs Sigmoid activation implemented via a symmetric piecewise linear approximation, as illustrated in Figure S6 of Supporting Information. Although operating at the same 50 MHz frequency, Model 2 achieves a shorter inference time (0.284 ms) due to its smaller parameter count. However, the LUT utilization reaches 75.63%, significantly higher than Model 1, because of the additional logic required for the piecewise Sigmoid module. This overhead also results in increased dynamic power consumption (482 mW). The synthesized results and resource utilization are summarized in Figure 9.

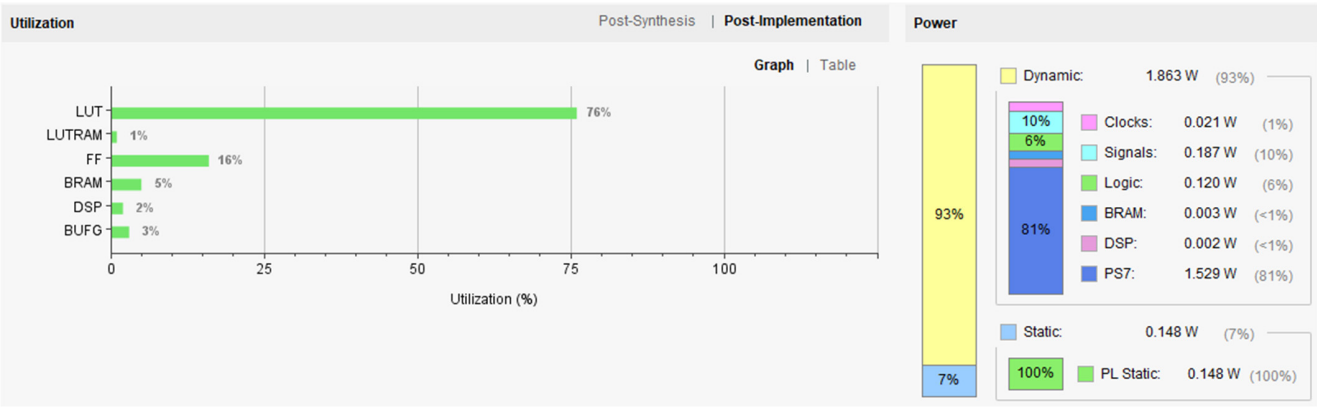



**Figure 9.** Resource utilization and power consumption evaluation of Model 2 accelerator.

The static power consumption of the two accelerators is similar (147 mW for Model 1 and 148 mW for Model 2). However, dynamic power differs considerably: Model 1 consumes 141 mW, whereas Model 2 requires 334 mW, resulting in total power consumptions of 288 mW and 482 mW, respectively. As summarized in Table 6, Model 1 demands substantially more BRAM due to its larger network size. LUTRAM usage remains identical because both accelerators share the same control architecture. In contrast, LUT usage increases markedly in Model 2 because of the piecewise Sigmoid module, leading to approximately 79% higher LUT consumption compared with Model 1.

**Table 6.** Comparison of resource utilization between the two accelerators.

| Resource | Utilization | | Available | | Utilization % | |
|---|---|---|---|---|---|---|
| | Model 1 | Model 2 | Model 1 | Model 2 | Model 1 | Model 2 |
| LUT | 22,480 | 40,237 | 53,200 | 53,200 | 42.26 | 75.63 |
| LUTRAM | 60 | 60 | 17,400 | 17,400 | 0.34 | 0.34 |
| FF | 21,113 | 16,832 | 106,400 | 106,400 | 19.84 | 15.82 |
| BRAM | 49.50 | 7.50 | 140 | 140 | 35.36 | 5.36 |
| DSP | 4 | 4 | 220 | 220 | 1.82 | 1.82 |
| BUFG | 1 | 1 | 32 | 32 | 3.13 | 3.13 |

For comparative evaluation, both networks were also executed on a 666 MHz embedded CPU, and the results were benchmarked against their FPGA implementations as summarized in Table 7. Model 2 experiences noticeable accuracy degradation on FPGA due to the piecewise Sigmoid approximation but performs efficiently in software because of its smaller network size. Overall, Model 1 is better suited for low-power, real-time embedded deployment, whereas Model 2 may be preferred when computational resources are abundant and power consumption is not a primary constraint.

**Table 7.** Parameter comparison of gas recognition network performance.

| | Operating Frequency (MHz) | Average Computation Time per Inference (ms) | | Power Consumption (mW) | Accuracy (%) |
|---|---|---|---|---|---|
| | | Measured | Simulated | | |
| Model 1—Fully Hardware Implementation | 50 | 2.208 | 2.175 | 288 | 98.59 |
| Model 2—Fully Hardware Implementation | 50 | 0.314 | 0.2836 | 482 | 81.63 |
| Model 1—Software Implementation | 666 | 2.6149 | —— | 1529 | 99.98 |
| Model 2—Software Implementation | 666 | 0.3715 | —— | 1529 | 98.53 |

## 6. Conclusions

MEMS semiconductor gas sensors serve as a core technology for low-cost and highly integrated gas-monitoring systems; however, their inherent cross-sensitivity limits accurate discrimination in multicomponent gas environments. To address this challenge, this work introduces a system-level enhancement strategy based on three-level tunable-amplitude driving, which enables multi-state excitation of MEMS sensors and virtualizes each sensor into four functional sensing channels, thereby substantially enriching sensing diversity without increasing the number of sensing elements.

In the data-processing pipeline, multi-level signal reconstruction, adaptive response-stage detection, and a dislocated sparse-sampling algorithm are integrated to enhance

feature diversity. This preprocessing framework expands the dataset size by a factor of 21, effectively alleviating overfitting and improving robustness in multi-gas recognition. At the application layer, an FPGA-based multilayer perceptron (MLP) accelerator is developed, achieving a recognition accuracy of 98.59% with an inference latency of 2.2 ms and a power consumption of 288 mW, demonstrating strong potential for real-time and energy-efficient deployment in embedded systems.

Compared with conventional gas recognition systems that rely on larger sensor arrays or more complex learning models, the proposed framework achieves competitive accuracy with fewer sensing elements and lower computational overhead. By combining virtual-sensor generation, enhanced preprocessing, and hardware-accelerated inference, this work establishes a unified and practical pathway for developing low-power combustible-gas monitoring systems suitable for resource-constrained environments.

The present study focuses on gas recognition rather than quantitative concentration analysis; therefore, a formal limit-of-detection characterization is not provided. The minimum detectable concentration is primarily governed by the intrinsic sensitivity of the employed MEMS sensors, as specified in the manufacturers' datasheets. Although the proposed baseline-tracking strategy improves robustness against short-term drift, systematic characterization of long-term drift behavior under amplitude-modulated operation will be addressed in future work, together with extensions toward quantitative concentration estimation and broader gas-mixture scenarios.

**Supplementary Materials:** The following supporting information can be downloaded at: https://www.mdpi.com/article/10.3390/chemosensors14030059/s1, Figure S1: Framework of the driving signal generation module; Figure S2: Schematic of the sensor array driving and data acquisition board; Figure S3: Schematic diagram of gas sample pre-mixing and gas testing process; Figure S4: Flowchart of the original gas response acquisition process; Figure S5: State transition diagram of the No. 1 network accelerator; Figure S6: Comparison diagram of hardware implementations of activation functions; Figure S7: Envelope curves of the 16 reconstructed virtual-sensor responses obtained from sample label No. 5. Each curve corresponds to a voltage-dependent operating state generated by the three-level amplitude-modulated driving waveform; Figure S8: Schematic diagram of the principle of the response-phase feature recognition algorithm; Figure S9: Identification results of the gas response phase; Figure S10: Schematic diagram of the dislocated sparse sampling–based dataset augmentation algorithm; Table S1: Comprehensive summary of training performance, model architecture, and computational characteristics for all gas-recognition networks evaluated in the experimental and control groups; Table S2: Comparison with recent temperature-/waveform-modulated gas recognition systems, including hardware and power characteristics.

**Author Contributions:** Conceptualization, M.J. and B.B.; Methodology, J.H. and F.J.; Software, J.H.; Validation, J.H. and F.J.; Formal analysis, Y.H.; Investigation, M.J.; Resources, Y.H.; Data curation, B.B.; Writing—original draft, J.H.; Writing—review & editing, M.J.; Visualization, F.J.; Supervision, M.J.; Project administration, Y.H.; Funding acquisition, Y.H. All authors have read and agreed to the published version of the manuscript.

**Funding:** This work was supported in part by the National Major Science and Technology Projects of China under Grant 2024ZD1004505, in part by the National Natural Science Foundation of China under Grant 62204260.

**Institutional Review Board Statement:** Not applicable.

**Informed Consent Statement:** Not applicable.

**Data Availability Statement:** Further inquiries of related data can be directed to the corresponding author.

**Conflicts of Interest:** The authors declare no conflict of interest.

## References


1. Zhai, Z.; Liu, Y.; Li, C.; Wang, D.; Wu, H. Electronic Noses: From Gas-Sensitive Components and Practical Applications to Data Processing. *Sensors* **2024**, *24*, 4806. [CrossRef]
2. Tibaduiza, D.; Anaya, M.; Gómez, J.; Sarmiento, J.; Perez, M.; Lara, C.; Ruiz, J.; Osorio, N.; Rodriguez, K.; Hernandez, I.; et al. Electronic Tongues and Noses: A General Overview. *Biosensors* **2024**, *14*, 190. [CrossRef]
3. Zong, B.; Wu, S.; Yang, Y.; Li, Q.; Tao, T.; Mao, S. Smart Gas Sensors: Recent Developments and Future Prospective. *Nano-Micro Lett.* **2025**, *17*, 54. [CrossRef] [PubMed]
4. Wilson, A.D.; Baietto, M. Advances in Electronic-Nose Technologies Developed for Biomedical Applications. *Sensors* **2011**, *11*, 1105–1176. [CrossRef] [PubMed]
5. Rabehi, A.; Helal, H.; Zappa, D.; Comini, E. Advancements and Prospects of Electronic Nose in Various Applications: A Comprehensive Review. *Appl. Sci.* **2024**, *14*, 4506. [CrossRef]
6. Yan, J.; Guo, X.; Duan, S.; Jia, P.; Wang, L.; Peng, C.; Zhang, S. Electronic Nose Feature Extraction Methods: A Review. *Sensors* **2015**, *15*, 27804–27831. [CrossRef]
7. Hotel, O.; Poli, J.-P.; Mer-Calfati, C.; Scorsone, E.; Saada, S. A Review of Algorithms for SAW Sensors E-Nose Based Volatile Compound Identification. *Sens. Actuators B Chem.* **2018**, *255*, 2472–2482. [CrossRef]
8. Ye, Z.; Liu, Y.; Li, Q. Recent Progress in Smart Electronic Nose Technologies Enabled with Machine Learning Methods. *Sensors* **2021**, *21*, 7620. [CrossRef] [PubMed]
9. Wang, X.; Zhou, Y.; Zhao, Z.; Feng, X.; Wang, Z.; Jiao, M. Advanced Algorithms for Low Dimensional Metal Oxides-Based Electronic Nose Application: A Review. *Crystals* **2023**, *13*, 615. [CrossRef]
10. Tereshkov, M.; Dontsova, T.; Saruhan, B.; Krüger, S. Metal Oxide-Based Sensors for Ecological Monitoring: Progress and Perspectives. *Chemosensors* **2024**, *12*, 42. [CrossRef]
11. Chen, H.; Huo, D.; Zhang, J. Gas Recognition in E-Nose System: A Review. *IEEE Trans. Biomed. Circuits Syst.* **2022**, *16*, 169–184. [CrossRef]
12. An, W.; Yang, C.Y. Review on Temperature Modulation Technology of Gas Sensors. *Appl. Mech. Mater.* **2011**, *143*, 567–571. [CrossRef]
13. Asri, M.I.A.; Hasan, M.N.; Fuaad, M.R.A.; Yunos, Y.M.; Ali, M.S.M. MEMS Gas Sensors: A Review. *IEEE Sens. J.* **2021**, *21*, 18381–18397. [CrossRef]
14. Mei, H.; Peng, J.; Wang, T.; Zhou, T.; Zhao, H.; Zhang, T.; Yang, Z. Overcoming the Limits of Cross-Sensitivity: Pattern Recognition Methods for Chemiresistive Gas Sensor Array. *Nano-Micro Lett.* **2024**, *16*, 269. [CrossRef] [PubMed]
15. Wu, Y.; Lei, M.; Xia, X. Research Progress of MEMS Gas Sensors: A Comprehensive Review of Sensing Materials. *Sensors* **2024**, *24*, 8125. [CrossRef]
16. Pan, J.; Yang, A.; Wang, D.; Chu, J.; Lei, F.; Wang, X.; Rong, M. Lightweight Neural Network for Gas Identification Based on Semiconductor Sensor. *IEEE Trans. Instrum. Meas.* **2022**, *71*, 1–8. [CrossRef]
17. Liang, H.; Long, Y.; Liu, G. Qualitative and Quantitative Studies of Multicomponent Gas by CNN-KPCA-RF Model. *Vib. Spectrosc.* **2024**, *130*, 103647. [CrossRef]
18. Zhang, H.; Ren, T.; Meng, F. Research on Binary Gas Intelligent Identification Method Based on Convolutional Neural Network and Temperature Dynamic Modulation. *Sens. Actuators B Chem.* **2024**, *418*, 136192. [CrossRef]
19. Luo, W.; Dai, F.; Liu, Y.; Wang, X.; Li, M. Pulse-Driven MEMS Gas Sensor Combined with Machine Learning for Selective Gas Identification. *Microsyst. Nanoeng.* **2025**, *11*, 72. [CrossRef]
20. Lee, B.; Kang, M.; Lee, K.; Chae, Y.; Yoon, K.-J.; Lee, D.-S.; Park, I. Multigas Identification by Temperature-Modulated Operation of a Single Anodic Aluminum Oxide Gas Sensor Platform and Deep Learning Algorithm. *ACS Sens.* **2025**, *10*, 954–964. [CrossRef]
21. Mei, H.; Peng, J.; Wang, T.; Wang, L.; Zhang, B.; Xuan, F. Overcoming Selectivity Challenges in Single Gas Sensor Leveraging Temperature Modulation and Multi-Feature Fusion. *Chem. Eng. J.* **2025**, *522*, 167722. [CrossRef]
22. Iwata, T.; Okura, Y.; Saeki, M.; Yoshikawa, T. Optimization of Temperature Modulation for Gas Classification Based on Bayesian Optimization. *Sensors* **2024**, *24*, 2941. [CrossRef]
23. Ye, B.; Zhang, M.; Jiang, B.; Du, B.; Tang, B.; Luo, B.; Shi, S.; Long, Z.; Wang, J.; Peng, X.; et al. Advances of Semiconductor Gas Sensor on Multi-Parameter Sensing and Features Extraction Methods. *Rev. Sci. Instrum.* **2025**, *96*, 121501. [CrossRef]
24. Ji, H.; Yuan, Z.; Zhu, H.; Qin, W.; Wang, H.; Meng, F. Dynamic Temperature Modulation Measurement of VOC Gases Based on SnO2 Gas Sensor. *IEEE Sens. J.* **2022**, *22*, 14708–14716. [CrossRef]
25. Hu, Z.; Zhao, W.; Cheng, H.; Yan, R.; Duan, X.; Yu, T.; Chen, Y.; Xu, D. Application of PSO-CNN Algorithm in Semiconductor Gas Sensors Based on Temperature Modulation. *IEEE Sens. J.* **2024**, *24*, 32717–32728. [CrossRef]
26. Wen, W.-C.; Chou, T.-I.; Tang, K.-T. A Gas Mixture Prediction Model Based on the Dynamic Response of a Metal-Oxide Sensor. *Micromachines* **2019**, *10*, 598. [CrossRef]
27. Pieniążek, J.; Cieciński, P.; Ficek, D.; Szumski, M. Dynamic Response of the Pitot Tube with Pressure Sensor. *Sensors* **2023**, *23*, 2843. [CrossRef] [PubMed]

28. Fan, Y.-H.; Chou, T.-I.; Chiu, S.-W.; Tang, K.-T. Gas Identification Algorithm Based on Dynamic Response Analysis of Metal Oxide Sensors Under Temperature Modulation. *IEEE Access* **2024**, *12*, 87900–87908. [CrossRef]
29. Dehnaw, A.M.; Lu, Y.-J.; Shih, J.-H.; Yao, C.-K.; Bitew, M.A.; Peng, P.-C. Deep Neural Network Optimization for Efficient Gas Detection Systems in Edge Intelligence Environments. *Processes* **2024**, *12*, 2638. [CrossRef]
30. Sun, F.; Wu, B.; Yan, J.; Duan, S.; Hu, X. Electronic Nose Pattern Recognition Engine: Design, Build, and Deployment. *IEEE Sens. J.* **2023**, *23*, 1507–1514. [CrossRef]
31. Shi, M.; Bermak, A.; Chandrasekaran, S.; Amira, A.; Brahim-Belhouari, S. A Committee Machine Gas Identification System Based on Dynamically Reconfigurable FPGA. *IEEE Sens. J.* **2008**, *8*, 403–414. [CrossRef]
32. Zhai, X.; Ali, A.A.S.; Amira, A.; Bensaali, F. MLP Neural Network Based Gas Classification System on Zynq SoC. *IEEE Access* **2016**, *4*, 8138–8146. [CrossRef]
33. Shi, Y.; Gong, F.; Wang, M.; Liu, J.; Wu, Y.; Men, H. A Deep Feature Mining Method of Electronic Nose Sensor Data for Identifying Beer Olfactory Information. *J. Food Eng.* **2019**, *263*, 437–445. [CrossRef]
34. Do A. Ferreira, A.P.; Da S. Barros, E.N. A High Performance Full Pipelined Arquitecture of MLP Neural Networks in FPGA. In *Proceedings of the 2010 17th IEEE International Conference on Electronics, Circuits and Systems*; IEEE: Athens, Greece, 2010; pp. 742–745.
35. Zhang, J.; Jiao, M.; Duan, L.; Zheng, L.; Nguyen, V.; Hung, C.M.; Nguyen, D. Gas Classification System Based on Hybrid Waveform Modulation Technology on FPGA. *Sens. Actuators B Chem.* **2025**, *435*, 137637. [CrossRef]
36. Kumar, A.; Pandey, G.; Kumar, R.; Yadav, J.; Mondal, S.; Molokitina, N.S. Fast Switching Hydrogen Gas Leakage Identification Using FPGA. *Int. J. Hydrogen Energy* **2024**, *69*, 1157–1165. [CrossRef]
37. Algamili, A.S.; Khir, M.H.; Ahmed, A.Y.; Rabih, A.A.; Ba-Hashwan, S.S.; Alabsi, S.S.; Al-Mahdi, O.L.; Isyaku, U.B.; Ahmed, M.G.; Junaid, M. Fabrication and Characterization of the Micro-Heater and Temperature Sensor for PolyMUMPs-Based MEMS Gas Sensor. *Micromachines* **2022**, *13*, 525. [CrossRef] [PubMed]
38. Hyeon, J.-S.; Kim, H.-J. Baseline Calibration Scheme Embedded in Single-Slope ADC for Gas Sensor Applications. *Electronics* **2024**, *13*, 1252. [CrossRef]
39. Wang, T.; Zhang, H.; Wu, Y.; Jiang, W.; Chen, X.; Zeng, M.; Yang, J.; Su, Y.; Hu, N.; Yang, Z. Target Discrimination, Concentration Prediction, and Status Judgment of Electronic Nose System Based on Large-Scale Measurement and Multi-Task Deep Learning. *Sens. Actuators B Chem.* **2022**, *351*, 130915. [CrossRef]


**Disclaimer/Publisher's Note:** The statements, opinions and data contained in all publications are solely those of the individual author(s) and contributor(s) and not of MDPI and/or the editor(s). MDPI and/or the editor(s) disclaim responsibility for any injury to people or property resulting from any ideas, methods, instructions or products referred to in the content.